Unraveling the Role of Order-to-Disorder Transition in Shear Thickening Suspensions

Jonghun Lee, Zhang Jiang, Jin Wang, Alec R. Sandy, and Suresh Narayanan*
Advanced Photon Source, Argonne National Laboratory, Argonne, Illinois 60439, USA

Xiao-Min Lin†
Center for Nanoscale Materials, Argonne National Laboratory, Argonne, Illinois 60439, USA

(Received 2 May 2017; revised manuscript received 16 November 2017; published 9 January 2018)

Using high-resolution *in situ* small angle x-ray scattering in conjunction with oscillatory shear on highly monodisperse silica suspensions, we demonstrate that an order-to-disorder transition leads to a dynamic shear thickening in a lower stress regime than the standard steady shear thickening. We show that the order-to-disorder transition is controlled by strain, which is distinguishably different from steady shear thickening, which is a stress-related phenomenon. The appearance of this two-step shear thinning and thickening transition is also influenced by the particle size, monodispersity, and measurement conditions (i.e., oscillatory shear versus steady shear). Our results show definitively that the order-to-disorder transition-induced thickening is completely unrelated to the mechanism that drives steady shear thickening.

DOI: 10.1103/PhysRevLett.120.028002

In a variety of colloidal suspensions, the transition from Newtonian to non-Newtonian behavior, including shear thinning and shear thickening, occurs with an increase of shear stress [1,2]. For discontinuous shear thickening, in which the suspension viscosity increases by orders of magnitude, it is increasingly clear that frictional contact between particles plays a key role in leading to a shear jamming state [3–6]. On the other hand, in continuous shear thickening (CST), where the viscosity increase is less than an order of magnitude, the picture still remains somewhat unclear [7–9]. Early studies attributed shear thinning to the formation of ordered structures in the suspension and shear thickening to the subsequent dissolution of these ordered structures [10–13]. Despite the fact that the formation of ordered structures under shear flow is often observed [14], especially under the oscillatory shear conditions [12,13,15–18], not all shear thickening fluids exhibit this type of order-to-disorder transition [19,20]. As a result, the order-to-disorder transition model was subsequently replaced by the so-called hydrocluster model proposed by Brady *et al.* [21,22]. Experimentally, the hydrocluster model is supported by results from neutron scattering [23–25] and confocal microscopy [26]. However, most recently, the importance of frictional contact between particles is being carefully scrutinized even in CST suspensions [7,27–29]. With this ongoing debate, the order-to-disorder transition has been lost in the shuffle. Its relationship with shear thickening remains somewhat ambiguous and has never been clearly elucidated [9,30].

Using *in situ* small angle x-ray scattering (SAXS), we studied the structural evolution of highly monodisperse dense silica particle suspensions with increasing shear stress during both oscillatory shear and steady shear. We show that, under oscillatory shear, these monodisperse suspensions exhibit a unique two-step dynamic shear thinning and thickening behavior. We demonstrate that the thickening at the lower critical stress is associated with an order-to-disorder transition which is strain related, whereas the thickening at the higher critical stress coincides with the standard shear thickening during steady shear. We find that the particle size, particle monodispersity, and measurement conditions affect the appearance of the order-to-disorder transition and in some cases can make it unobservable. Our results provide new insight into the relationship between the order-to-disorder transition and shear thickening and clarify why certain shear thickening fluids show this transition whereas others do not.

For *in situ* SAXS measurements, a stress-controlled rheometer (Anton-Paar MCR 301) was installed at beam line 8-ID-I at the Advanced Photon Source. Figure 1(a) shows a schematic of the experimental geometry. A collimated x-ray beam (7.4 keV, 20 μm in width and height) passes through the center of the polycarbonate Couette cell, perpendicular to the rotational axis of the cell. The x-ray beam is along the shear gradient direction and the scattering pattern is collected in the velocity-vorticity plane using a 2D CCD detector. Silica particles of three different sizes (diameter ~155, ~360, and ~460 nm) were synthesized using the standard Stöber method and were dispersed in polyethylene glycol (molar mass = 200 g/mol) with various volume fractions. (For more details, see Supplemental Material [31].) We will mainly focus on the suspension of 360 nm particles with a volume fraction of 56.3%, unless stated otherwise. The highly monodisperse nature of the particles is evident from both the transmission electron microscopy (TEM) image [Fig. 1(a)] and the many orders of

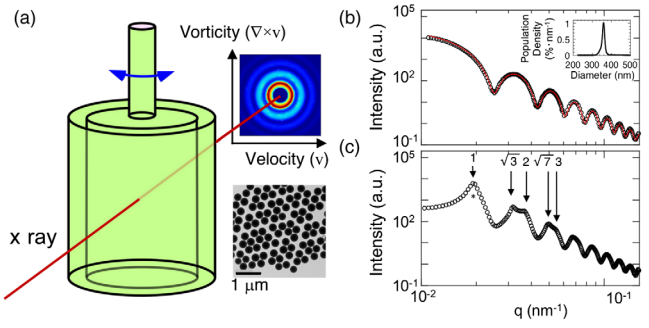

FIG. 1. Particle monodispersity and quiescent structure for a 360 nm particle suspension. (a) Schematic of the *in situ* SAXS setup. The lower-right inset is a TEM image of the particles. (b) The form factor of the particles measured from a 1% volume fraction solution by SAXS. Black circles are experimental data, and the red line is the fitting curve yielding a standard deviation of 14 nm shown in the inset. (c) $I(q)$ versus q curve measured using a suspension with 56.3% volume fraction in its quiescent state.

oscillations in the particle form factor measured by SAXS [Fig. 1(b)]. Fitting the form factor yields both the average particle size (360 nm) and particle size distribution (standard deviation of 14 nm).

The silica particles behave like hard spheres, so the sample with a volume fraction of 56.3% is in the crystalline regime under equilibrium conditions [32,33]. Right after preshear, a few crystallites nucleated immediately as evidenced from the strong diffraction spots appearing atop the amorphous scattering ring in the quiescent state SAXS pattern (Fig. S1 in Supplemental Material [31]). The azimuthally averaged scattering intensity [Fig. 1(c)] shows that the ratio of the first five scattering peaks is close to $1:\sqrt{3}:2:\sqrt{7}:3$. This specific ratio indicates that the crystallites have likely formed on the cell wall, hexagonally close packed, with the c axis aligned with the x-ray beam direction but randomly oriented in the other two directions [34]. Therefore, the position of the first peak, indicated by an asterisk (*) in Fig. 1(c), is associated with the first-order crystalline peak rather than the interparticle spacing in a disordered solid.

Rheological measurements were conducted under both steady shear and oscillatory shear at different frequencies (0.1, 1, and 5 Hz) with increasing strain amplitude [Fig. 2(a)]. For both types of shear, the silica suspension shows yielding behavior, consistent with the fact that the suspension is in a solid phase [35]. Under steady shear, the suspension shows a single-step shear thinning to thickening transition, whereas under oscillatory shear, it exhibits a more complex behavior that has not been observed before [17,30,36,37]. For frequencies of 0.1 and 1 Hz, the complex viscosity η^* versus stress curves show a two-step dynamic shear thinning to thickening behavior, occurring at two different critical shear stress values (τ_L^* and τ_H^*). As the oscillation frequency increases, τ_L^* shifts to higher stress values, while $\tau_H^* \sim 120$ Pa is independent of the frequency and coincides with the critical stress for shear thickening during steady shear. At 5 Hz, τ_L^* increases to the point that the two shear thinning to thickening processes merge and appear to become a single process. Beyond τ_H^*, all the oscillatory shear curves are nearly of the same magnitude in viscosity as observed under steady shear. The same behavior was also observed using a cone-plate and a plate-plate geometry (Fig. S2 in Supplemental Material [31]), indicating that it does not depend upon the testing geometry.

To understand the parameters that affect the two-step shear thinning to thickening behavior during oscillatory shear, we studied the rheological behaviors of suspensions under different conditions: three different sizes of particles (460, 360, and 155 nm) at two different packing fractions (56.3% and 51.2%). The 460 and 360 nm suspensions with 56.3% and 51.2% volume fractions show similar two-step shear thinning to thickening behavior at all frequencies (Figs. S3–S5 in Supplemental Material [31]). In contrast, a suspension of 155 nm particles at 56.3% volume fraction shows only a single-step transition at all measured frequencies [Fig. 2(b)]. Only when the volume fraction is decreased to 51.2% and oscillation frequency is 5 Hz does this suspension exhibit the two-step shear thinning to thickening behavior [Fig. S3(a) in Supplemental Material [31]]. Table I summarizes the linear viscoelastic properties of the

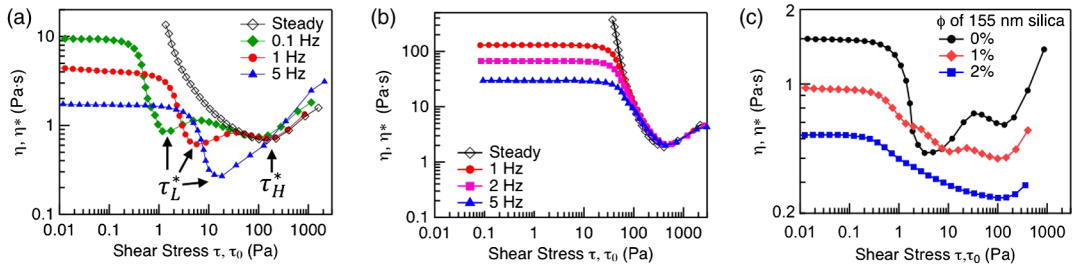

FIG. 2. Rheological data during oscillatory and steady shear. (a) Viscosity (η) and complex viscosity (η^*) versus shear stress under steady and oscillatory shear (0.1, 1, and 5 Hz) for 360 nm particles at 56.3% volume fraction. For oscillatory shear, the shear stress is the maximum shear stress τ_0 applied during each oscillatory cycle. (b) The same type of measurements as (a), but for 155 nm particles at 56.3% volume fraction. (c) Oscillatory shear for 340 nm particles at 1 Hz at 56.3% volume fraction, with different amounts of 155 nm particles mixed in [note: a different set of samples than those shown in (a), but with similar monodispersity].

TABLE I. Linear viscoelastic properties of silica suspensions of three different particle sizes with two different volume fractions measured at different frequencies. f is the oscillation frequency, τ_{yield} is the yield stress, G_0' is the storage modulus in the linear regime, and $\tan\delta = G_0''/G_0'$ is the loss tangent, in which G_0'' is the loss modulus in the linear regime. For $G_0' > G_0''$, the yield stress is defined as the stress at the crossover between G' and G'', whereas for $G_0' < G_0''$, it is defined as the crossover between two tangential lines drawn on G', one in the linear regime and another one in the shear thinning regime. The bold regime indicates where a two-step dynamic shear thinning and thickening was observed.

	155 nm				360 nm				460 nm			
	f (Hz)	τ_{yield} (Pa)	G_0' (Pa)	$\tan\delta$	f (Hz)	τ_{yield} (Pa)	G_0' (Pa)	$\tan\delta$	f (Hz)	τ_{yield} (Pa)	G_0' (Pa)	$\tan\delta$
	1	50	816	0.12	**0.1**	**0.4**	**5.6**	**0.34**	**1**	**0.3**	**5.3**	**0.84**
56.3%	2	56	834	0.15	**1**	**1.8**	**23**	**0.44**	**2**	**0.7**	**5.2**	**1.16**
	5	77	916	0.17	**5**	**4.0**	**46**	**0.58**	**5**	**1.8**	**7.1**	**1.60**
	1	20	252	0.17	**1**	**0.3**	**3.5**	**0.90**	**1**	**0.3**	**1.7**	**1.36**
51.2%	2	22	270	0.20	**2**	**0.3**	**3.7**	**1.30**	**2**	**0.5**	**2.5**	**1.49**
	5	**29**	**278**	**0.24**	5	**0.24**	**7.7**	**1.24**	5	···	**1.5**	**4.25**

silica suspensions (see also Figs. S6 and S7 in Supplemental Material for all strain sweep and frequency sweep data [31]). Generally, we find that suspensions with a relatively low yield stress and high loss tangent exhibit the two-step shear thinning to thickening behavior while the ones that show strong elastic solid behavior do not.

Monodispersity is also an important factor for the appearance of two-step shear thinning to thickening behavior during oscillatory shear. An earlier oscillatory shear experiment by Lee and Wagner used a similar type of silica particle suspension, but, unlike the data presented above, only a single shear thinning to thickening event was observed [36]. We suspected that the bimodal size distribution of the silica nanoparticles used in the earlier study could be a contributing factor. To test this hypothesis, we mixed small fractions of 155 nm particles into a 340 nm particle dispersion while keeping the overall volume fraction of the particles the same at 56.3%. Figure 2(c) shows that, at a 1% volume fraction of smaller particles, the two-step viscosity feature is significantly weakened, while at 2% the two-step viscosity feature completely disappears. This proves that a high degree of sample monodispersity is crucial for observing this unique behavior.

To elucidate the microstructural origin of this rheological behavior, we measured *in situ* SAXS of the suspensions under oscillatory shear. The experiments were carried out at a fixed strain amplitude and frequency, and the SAXS patterns were collected over ~200 oscillation cycles and then averaged together. Figure 3(a) shows the steady and oscillatory shear curves for 360 nm particles at 1 Hz. Arrows indicate the different shear stresses where x-ray scattering was measured during oscillatory shear, and the corresponding SAXS patterns are shown in Fig. 3(b).

Even with a small applied shear stress, ca. 0.03 Pa, a well-defined sixfold scattering pattern appears [Fig. 3(b1)]. This shows that the randomly oriented crystallites in the quiescent state begin to reorient themselves in the velocity-vorticity plane in response to the shear. These crystallites serve as nucleation centers for further growth of the ordered structures. As the oscillatory shear stress is increased, the

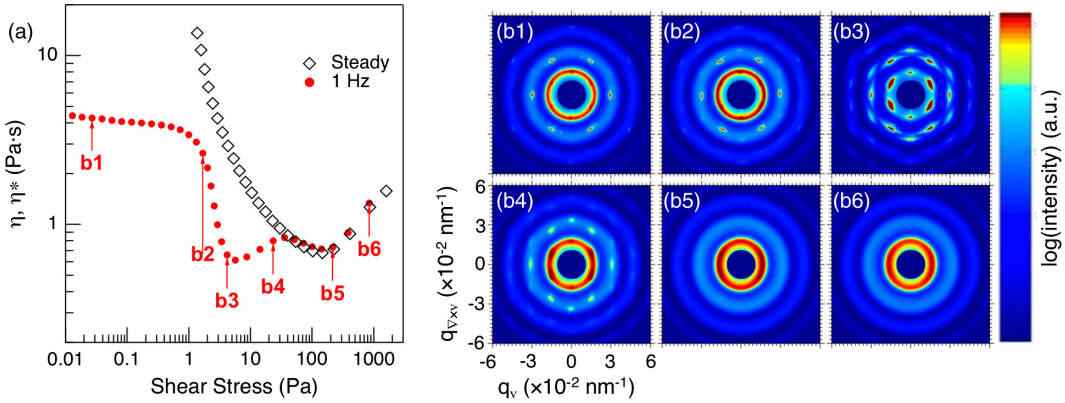

FIG. 3. Scattering patterns during oscillatory shear at 1 Hz. (a) Rheological data of a 360 nm silica dispersion with a volume fraction of 56.3%. (b) SAXS patterns of this dispersion at different oscillatory shear stresses at 1 Hz. For (b1)–(b6), the labels correspond to different points indicated in (a). **q** is the scattering vector, v denotes the velocity direction, and $\nabla \times v$ denotes the vorticity direction. The scattering intensity is plotted on a log scale.

sixfold scattering pattern becomes more pronounced, indicating that more particles are now in the ordered regions. At τ_L^*, the sixfold scattering pattern is most distinct [Fig. 3(b3)], but the two peaks along the vorticity direction are weaker than the other four peaks. This scattering pattern is caused by the formation of so-called sliding layers, namely, layers of hexagonally close-packed particles sliding past each other, perpendicular to the shear gradient [13,18,19,38,39]. Similar scattering patterns were observed using other particle sizes and frequencies, as long as the system displayed the two-step shear thinning to thickening rheologically. Plotting the same data against the strain amplitude revealed that the transition at τ_L^* occurs at the same critical strain amplitude ($\sim$1), regardless of the particle size and oscillation frequency (Fig. S4 in Supplemental Material [31]). Similar behavior was observed by several other groups [12,15,17]. Rheologically, it is mainly associated with an upturn of both elastic and loss modulus at this critical strain, akin to strain hardening in a typical extensional rheology experiment. Interestingly, we found that, even though high strain or stress can melt the sliding layers completely [Figs. 3(b4)–3(b6)], upon reversing the strain sweep the ordered structures reappear, albeit at a slightly different critical strain (see Fig. S8 in Supplemental Material [31]). When the strain amplitude is reduced to almost zero, crystalline structures still remain and the corresponding viscosity is lower than its initial state. A similar hysteretic order-to-disorder transition was previously observed by Koumakis, Schofield, and Petekidis [17].

To analyze the degree of ordering, we fit the integrated scattering intensity data versus the azimuthal angle (ϕ) using a linear combination of two contributions, one from an amorphous phase ($I_{\text{amorphous}}$) and another from a crystalline phase ($I_{\text{crystalline}}$). As the scattering from the amorphous phase is likely isotropic, it is assumed to be constant over ϕ. The crystalline peaks are best fit with a Voigt distribution. The relative degree of crystallinity of the sample can be defined as $I_R = I_{\text{crystalline}}/(I_{\text{crystalline}} + I_{\text{amorphous}})$. The change of I_R over the entire stress range at 1 Hz shows a direct correlation between the degree of ordering and the change of viscosity, with the highest ordering occurring at τ_L^* (see Figs. S9 and S10 in Supplemental Material [31]). As the oscillation frequency increases, an increasing fraction of particles are organized into the sliding layer structure, with I_R changing from 0.41 (at 0.1 Hz), 0.67 (at 1 Hz), and to 0.94 (at 5 Hz) [Fig. 4]. This indicates that, although the order-to-disorder transition is strain related, the frequency does play a role, resulting in a different viscosity at τ_L^* as shown in Fig. 2(a).

An important observation in Fig. 2(a) is that steady shear leads to only one shear thinning to thickening step, with the critical stress occurring at τ_H^*. *In situ* SAXS during steady shear confirmed that the system bypasses the order-to-disorder transition entirely without the formation of the

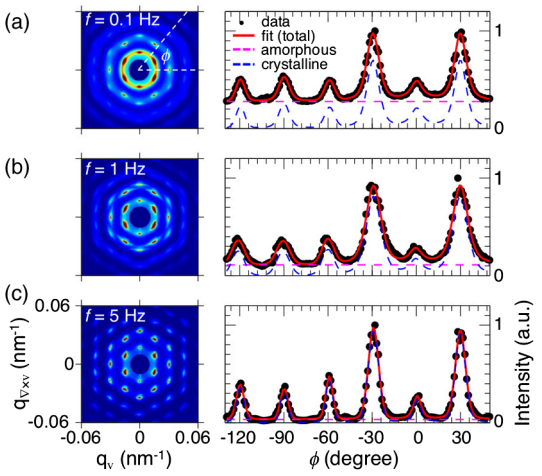

FIG. 4. Sliding layer structures formed at τ_L^* by an oscillatory shear at frequencies of (a) 0.1, (b) 1, and (c) 5 Hz for a 360 nm particle suspension at 56.3% volume fraction, where τ_L^* is 1.4, 4.7, and 11.3 Pa, respectively. The left panels are the scattering patterns at each τ_L^*. The right panels are the integrated scattering intensities plotted against the azimuthal angle ϕ.

sliding layer (Fig. S11 in Supplemental Material [31]). The fact that we are able to clearly distinguish the order-to-disorder transition, which occurs at different critical stresses (τ_L^*) than the steady shear critical stress τ_H^*, indicates several important facts: (i) The strain-induced sliding layer formation can greatly reduce the viscosity during oscillatory shear, causing the system to adopt a lower viscosity curve than the steady shear [18,19,32]. On the other hand, for systems that do not form sliding layers, the complex viscosity curve merges with the steady shear curve immediately beyond the yield stress and follows the extended Cox-Merz rule $\eta^*(\gamma_0\omega) = \eta(\dot{\gamma})|_{\dot{\gamma}=\gamma_0\omega}$ [Fig. 2(b)] [40]. (ii) The mechanism for shear thickening near the high critical shear stress τ_H^* is intrinsically different and not related to the order-to-disorder transition at τ_L^*. The onset stress for the shear thickening at τ_H^* is independent of how suspensions are sheared, i.e., either by steady shear or by oscillatory shear. For both shear modes, similar anisotropic SAXS patterns were observed in the regime $\tau > \tau_H^*$ (Fig. S12 in Supplemental Material [31]), which indicates that the microscopic origin for this stress-controlled shear thickening is the same. Although the long-standing interpretation of continuous shear thickening is the flow-induced hydrocluster model [20–26], in the q range of this study, the change in the first-order structure factor peak is too small to indicate significantly large cluster formation. An alternative interpretation is that shear thickening in this regime involves a stress-induced transition from lubrication to frictional contact [4–6,8,27,28]. This model has been recently extended from large non-Brownian particles to small Brownian particles by Guy, Hermes, and Poon [29]. Similar to their PMMA particle system, our silica suspensions show critical stress τ_H^* scales as d^{-2}, where d is the

particle diameter (Fig. S13 in Supplemental Material [31]). (iii) The appearance of order-to-disorder-induced shear thickening largely depends on the sample and measurement conditions. It appears only in monodisperse suspensions that do not show strong elastic solid behavior (i.e., low yield stress and high loss tangent), in which particles can easily shear past one another to induce ordered structures. Our data also show that oscillatory shear is more likely to induce ordered structures, whereas, in the same system, steady shear can bypass the transition entirely. In other cases, the order-to-disorder transition can be masked by the large yield stress or the shear thickening at τ_H^*. Taking advantage of our monodisperse system, for the first time, we are able to unequivocally distinguish the shear thickening caused by the order-to-disorder transition from the steady shear thickening, thus clearly confirming that the latter phenomenon is driven by other mechanisms.

We acknowledge the expert technical assistance of M. Fisher and R. Ziegler and helpful discussions with B. Leheny, M. Sutton, and H. M. Jaeger. This work was performed at sector 8-ID-I at the Advanced Photon Source and the Center for Nanoscale Materials, U.S. Department of Energy, Office of Science, Office of Basic Energy Sciences User Facilities under Contract No. DE-AC02-06CH11357. J. L. acknowledges financial support from Argonne's LDRD program. X.-M. L. acknowledges partial support from the Chicago MRSEC, under NSF No. DMR-1420709.

*sureshn@anl.gov
†xmlin@anl.gov

[1] R. G. Larson, *The Structure and Rheology of Complex Fluids* (Oxford University, New York, 1999).
[2] J. Mewis and N. Wagner, *Colloidal Suspension Rheology* (Cambridge University Press, Cambridge, England, 2013).
[3] I. R. Peters, S. Majumdar, and H. M. Jaeger, Nature (London) **532**, 214 (2016).
[4] R. Seto, R. Mari, J. F. Morris, and M. M. Denn, Phys. Rev. Lett. **111**, 218301 (2013).
[5] M. Wyart and M. E. Cates, Phys. Rev. Lett. **112**, 098302 (2014).
[6] C. Clavaud, A. Bérut, B. Metzger, and Y. Forterre, Proc. Natl. Acad. Sci. U.S.A. **114**, 5147 (2017).
[7] N. Y. C. Lin, B. M. Guy, M. Hermes, C. Ness, J. Sun, W. C. K. Poon, and I. Cohen, Phys. Rev. Lett. **115**, 228304 (2015).
[8] N. Fernandez, R. Mani, D. Rinaldi, D. Kadau, M. Mosquet, H. Lombois-Burger, J. Cayer-Barrioz, H. J. Herrmann, N. D. Spencer, and L. Isa, Phys. Rev. Lett. **111**, 108301 (2013).
[9] E. Brown and H. M. Jaeger, Rep. Prog. Phys. **77**, 046602 (2014).
[10] R. L. Hoffman, Trans. Soc. Rheol. **16**, 155 (1972).
[11] R. L. Hoffman, J. Rheol. **42**, 111 (1998).
[12] B. J. Ackerson and P. N. Pusey, Phys. Rev. Lett. **61**, 1033 (1988).
[13] Y. D. Yan, J. K. G. Dhont, C. Smits, and H. N. W. Lekkerkerker, Physica A (Amsterdam) **202**, 68 (1994).
[14] J. Vermant and M. Solomon, J. Phys. Condens. Matter **17**, R187 (2005).
[15] M. D. Haw, W. C. K. Poon, P. N. Pusey, P. Hebraud, and F. Lequeux, Phys. Rev. E **58**, 4673 (1998).
[16] L. Chen, M. Chow, B. Ackerson, and C. Zukoski, Langmuir **10**, 2817 (1994).
[17] N. Koumakis, A. B. Schofield, and G. Petekidis, Soft Matter **4**, 2008 (2008).
[18] T. H. Besseling, M. Hermes, A. Fortini, M. Dijkstra, A. Imhofa, and A. van Blaaderen, Soft Matter **8**, 6931 (2012).
[19] H. M. Laun, R. Bung, S. Hess, W. Loose, O. Hess, K. Hahn, E. Hädicke, R. Hingmann, F. Schmidt, and P. Lindner, J. Rheol. **36**, 743 (1992).
[20] N. J. Wagner and J. F. Brady, Phys. Today **62**, No. 10, 27 (2009).
[21] J. F. Brady and G. Bossis, J. Fluid Mech. **155**, 105 (1985).
[22] D. R. Foss and J. F. Brady, J. Fluid Mech. **407**, 167 (2000).
[23] B. J. Maranzano and N. J. Wagner, J. Chem. Phys. **117**, 10291 (2002).
[24] A. K. Gurnon and N. J. Wagner, J. Fluid Mech. **769**, 242 (2015).
[25] Y. S. Lee and N. J. Wagner, Ind. Eng. Chem. Res. **45**, 7015 (2006).
[26] X. Cheng, J. H. McCoy, J. N. Israelachvili, and I. Cohen, Science **333**, 1276 (2011).
[27] F. Boyer, E. Guazzelli, and O. Pouliquen, Phys. Rev. Lett. **107**, 188301 (2011).
[28] J. R. Royer, D. L. Blair, and S. D. Hudson, Phys. Rev. Lett. **116**, 188301 (2016).
[29] B. M. Guy, M. Hermes, and W. C. K. Poon, Phys. Rev. Lett. **115**, 088304 (2015).
[30] X. Xu, S. Rice, and A. Dinner, Proc. Natl. Acad. Sci. U.S.A. **110**, 3771 (2013).
[31] See Supplemental Material at http://link.aps.org/supplemental/10.1103/PhysRevLett.120.028002 for details on synthesis and the experimental setup as well as additional data.
[32] P. N. Pusey, E. Zaccarelli, C. Valeriani, E. Sanz, W. C. K. Poon, and M. E. Cates, Phil. Trans. R. Soc. A **367**, 4993 (2009).
[33] U. Gasser, J. Phys. Condens. Matter **21**, 203101 (2009).
[34] B. D. Cullity and S. R. Stock, *Elements of X-Ray Diffraction* (Pearson, Columbus, OH, 2001).
[35] A. Fall, N. Huang, F. Bertrand, G. Ovarlez, and D. Bonn, Phys. Rev. Lett. **100**, 018301 (2008).
[36] Y. S. Lee and N. J. Wagner, Rheol. Acta **42**, 199 (2003).
[37] L. Chang, K. Friedrich, A. K. Schlarb, R. Tanner, and L. Ye, J. Mater Sci. **46**, 339 (2011).
[38] B. J. Ackerson, J. Rheol. **34**, 553 (1990).
[39] C. R. López-Barrón, N. J. Wagner, and L. Porcar, J. Rheol. **59**, 793 (2015).
[40] D. Doraiswamy, A. N. Mujumdar, I. Tsao, A. N. Beris, S. C. Danforth, and A. B. Metzner, J. Rheol. **35**, 647 (1991).